INTERNATIONAL JOURNAL FOR NUMERICAL METHODS IN ENGINEERING
Int. J. Numer. Meth. Engng 2015; **104**:749–766
Published online 10 June 2015 in Wiley Online Library (wileyonlinelibrary.com). DOI: 10.1002/nme.4937

A return mapping algorithm for unified strength theory model

Chen Lin and Yue-Ming Li*,†

State Key Laboratory for Strength and Vibration of Mechanical Structures, School of Aerospace Engineering, Xi'an Jiaotong University, Xi'an, 710049, China

SUMMARY

A return mapping algorithm in principal stress space for unified strength theory (UST) model is presented in this paper. In contrast to Mohr–Coulomb and Tresca models, UST model contains two planes and three corners in the sextant of principal stress space, and the apex is formed by the intersection of 12 corners rather than the six corners of Mohr–Coulomb in the whole principal stress space. In order to utilize UST model, the existing return mapping algorithm in principal stress space is modified. The return mapping schemes for one plane, middle corner, and apex of UST model are derived, and corresponding consistent constitutive matrices in principal stress space are constructed. Because of the flexibility of UST, the present model is not only suitable for analysis based on the traditional yield functions, such as Mohr–Coulomb, Tresca, and Mises, but might also be used for analysis based on a series of new failure criteria. The accuracy of the present model is assessed by the iso-error maps. Three numerical examples are also given to demonstrate the capability of the present algorithm. Copyright © 2015 John Wiley & Sons, Ltd.

Received 31 August 2012; Revised 8 April 2015; Accepted 12 April 2015

KEY WORDS: return mapping; corners; apex; unified strength theory (UST)

1. INTRODUCTION

Strength theory plays an important role in the elasto-plastic analyses of materials and structures. It is difficult to find a universal law for various materials in complex stress state. Up to now, many versions of strength theory have been developed. For instance, Tresca and von Mises, which have identical strength both in tension and compression, are two widely used strength theories for metallic materials. Mohr–Coulomb theory is widely applied in the analyses of failure of nonmetallic materials, because it considers the different strengths in tension and compression (i.e., strength difference (SD) effect) of nonmetallic materials, and the effect of hydrostatic pressure for nonmetallic materials. However, the disadvantage of these theories is that the intermediate principal stress is not taken into account. Many experiments, such as the true tri-axial test and the combined tension–torsion test, confirm that the effect of intermediate principal stress is an important characteristic of materials [1, 2]. And von Mises strength theory can only be adopted for non-SD materials with the ratio of the shear strength to the tensile strength of 0.577. Several strength theories for geo-materials take SD effect, the effect of hydrostatic pressure and the effect of intermediate principal stress into account, such as the William and Warnke [3], Hoek and Brown [4], and Lade and Duncan strength theories [5]. However, those theories are complex for the application in theory and numerical analyses. In addition, they are only suitable for special materials, for example, concrete and sand.

*Correspondence to: Yue-Ming Li, State Key Laboratory for Strength and Vibration of Mechanical Structures, School of Aerospace Engineering, Xi'an Jiaotong University, Xi'an, 710049, China.
†E-mail: liyueming@mail.xjtu.edu.cn

Unified strength theory (UST) is able to reflect the fundamental characteristics of isotropic materials, i.e., SD effect, the effects of intermediate principal stress, and hydrostatic pressure [6]. The yield loci of UST cover all the convex regions from Mohr–Coulomb theory to twin-shear strength theory; and a series of previous yield criteria, failure models, and other smooth criteria or empirical criteria can be obtained as special cases or linear approximations of UST. In addition, the formulation of UST is very simple and convenient to be adopted for closed-form analyses of various classical elasto-plastic problems. The yield surfaces of UST are piecewise linear including corners and apex, so that the standard normality rule is not applicable at the corners and apex, and the Koiter's generalized flow rule [7] based on the concept of sub-differential is employed.

Some methods [8], which smooth the corners using very complex mathematical models, have been proposed to eliminate the singularity of plastic flow for piecewise linear yield functions. There is, however, no need for smoothening of singular points for the UST. Another method suggested by Yu [9] is applied in finite element analyses, in which the plastic flow vectors at the corners could be determined by initial yield surfaces at every iteration step, so it is only suitable for the explicit Euler integration algorithm [10]. The final stress state might not satisfy the yield condition strictly, and the accuracy of numerical solution is strongly dependent on the iteration step length.

Another approach to solve the problems is to carry out the return mapping algorithm, a kind of implicit Euler integration algorithm, in principal stress space. In this way, the plastic flow vectors at the corners and apex can be determined easily and exactly. In addition, the principal stress-based algorithm results in a simpler and more effective computational implementation of piecewise linear models. The works of Pankaj and Bicanic [11], Larsson and Runesson [12], Perić and Neto [13], and Borja [14] and Clausen J [15, 16] all deal with the stress return in principal stress space for various plasticity models. The derivations and results in these works are based on the specific strength theories, for example, Tresca or Mohr–Coulomb.

In this paper, a return mapping algorithm in principal stress space for UST is developed. Because of the flexibility of UST, the present model is not only suitable for analysis based on the traditional yield functions, such as Mohr–Coulomb, Tresca, and Mises, but might also be used for analysis based on a series of new failure criteria. In the derivation of the algorithm, the plastic flow rule is taken to be associated; the linear isotropic hardening plasticity are assumed. The accuracy of the return mapping algorithm for UST model is assessed by the iso-error maps, and three numerical examples are also carried out to demonstrate the capability of the present model.

2. UNIFIED STRENGTH THEORY MODEL

In contrast to other piecewise linear yield criteria, the mathematical formulation of UST is bilinear in the sextant of principal stress space $\sigma_1 \geqslant \sigma_2 \geqslant \sigma_3$. The expression is given as follows

$$F \equiv \sigma_1 - \frac{\alpha}{1+b}(b\sigma_2 + \sigma_3) = \sigma_t, \text{ when } \sigma_2 \leqslant \frac{\sigma_1 + \alpha\sigma_3}{1+\alpha} \tag{2.1}$$

$$F' \equiv \frac{1}{1+b}(\sigma_1 + b\sigma_2) - \alpha\sigma_3 = \sigma_t, \text{ when } \sigma_2 \geqslant \frac{\sigma_1 + \alpha\sigma_3}{1+\alpha} \tag{2.2}$$

where σ_t is the tensile yield strength, α is the tension-compressive strength ratio to reflect SD effect, and b is a parameter that describes the effect of the intermediate principal stress on the failure of material. As shown in Figure 1, a series of convex failure criteria can be obtained when the parameter b varies from 0 to 1. Mohr–Coulomb strength theory can be derived from UST with $b = 0$. Other linear/nonlinear yield surfaces criteria can be described or linearly approximated by UST when $0.0 < b \leqslant 1.0$.

DOI: 10.1002/nme

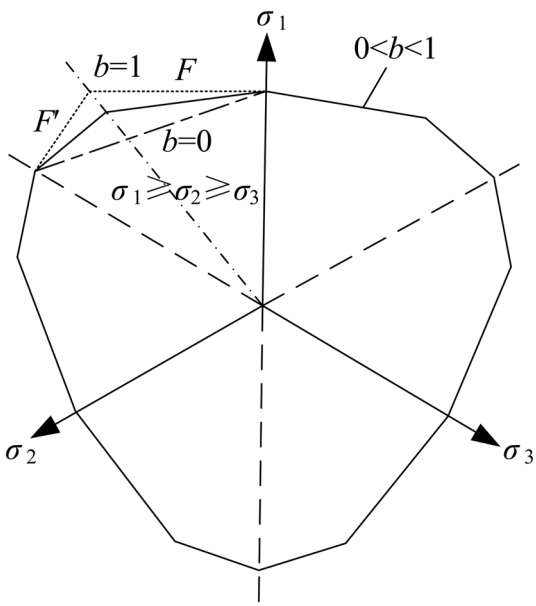

Figure 1. Yield loci of UST.

3. THE FRAMEWORK OF RETURN MAPPING ALGORITHM FOR UNIFIED STRENGTH THEORY MODEL

The return mapping algorithm based on principal stress space is a very simple and efficient numerical scheme in finite element implementations for piecewise linear yield models and is adopted for some classical strength criteria, such as Mohr–Coulomb and Tresca [17]. The yield surfaces of Mohr–Coulomb and Tresca contain one plane (surface), two corners, i.e., the right corner ($\sigma_1 = \sigma_2 > \sigma_3$), the left corner ($\sigma_1 > \sigma_2 = \sigma_3$), and an apex ($\sigma_1 = \sigma_2 = \sigma_3$) in the sextant of principal stress space $\sigma_1 \geqslant \sigma_2 \geqslant \sigma_3$. UST comprises two planes (surfaces) in the sextant of principal stress space $\sigma_1 \geqslant \sigma_2 \geqslant \sigma_3$ because of its bilinear mathematical expression. Because of the intersection of the two yield surfaces, another corner is formed in addition to the right and left corners. Furthermore, the apex is formed by the intersection of 12 corners for UST model rather than the six corners of Mohr–Coulomb in the whole principal stress space. These geometrical characteristics of yield surfaces of UST make the return mapping algorithm based on principal stress space different from other piecewise linear yield models.

In the present work, the framework of return mapping algorithm for UST model is carried out as follows.

The first procedure of the algorithm is the calculation of the elastic trial stresses in general stress space and the transformation of the trial stresses from general stress space to principal stress space [16]. From the first procedure, the three principal trial stresses are calculated and arranged as $\sigma_1^{\text{trial}} \geqslant \sigma_2^{\text{trial}} \geqslant \sigma_3^{\text{trial}}$, then the yield condition is checked with the following equations:

$$F^{\text{trial}} = \sigma_1^{\text{trial}} - \frac{a}{1+b}\left(b\sigma_2^{\text{trial}} + \sigma_3^{\text{trial}}\right) - \sigma_t^0 \leqslant 0, \text{ when } \sigma_2^{\text{trial}} \leqslant \frac{\sigma_1^{\text{trial}} + \alpha\sigma_3^{\text{trial}}}{1+\alpha} \tag{3.1}$$

$$F'^{\text{trial}} = \frac{1}{1+b}\left(\sigma_1^{\text{trial}} + b\sigma_2^{\text{trial}}\right) - a\sigma_3^{\text{trial}} - \sigma_t^0 \leqslant 0, \text{ when } \sigma_2^{\text{trial}} \geqslant \frac{\sigma_1^{\text{trial}} + \alpha\sigma_3^{\text{trial}}}{1+\alpha} \tag{3.2}$$

where σ_t^0 is the initial tensile yield strength at the current step.

DOI: 10.1002/nme

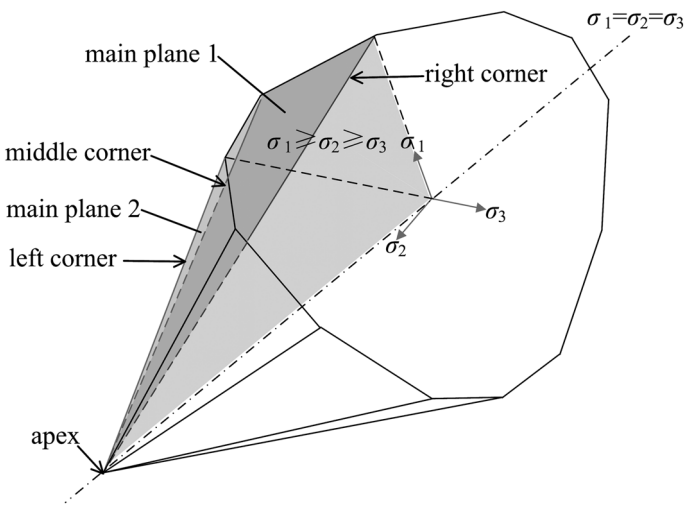

Figure 2. Six different stress return possibilities.

If Equation (3.1) or (3.2) is satisfied, the elastic trial stresses would lie on or within the yield surfaces of UST. The elastic calculation scheme should be carried out at this iteration step. Otherwise, a return mapping step must be applied to make the elastic trial stresses relax onto the suitably updated yield surfaces. As illustrated in Figure 2, there are six different return possibilities in the sextant of principal stress space $\sigma_1 \geqslant \sigma_2 \geqslant \sigma_3$ for UST model.

- Return to the main plane 1
- Return to the main plane 2
- Return to the left corner ($\sigma_1 > \sigma_2 = \sigma_3$)
- Return to the middle corner ($\sigma_1 - \sigma_2 = a(\sigma_2 - \sigma_3)$ and $\sigma_1 \geqslant \sigma_2 \geqslant \sigma_3$)
- Return to the right corner ($\sigma_1 = \sigma_2 > \sigma_3$)
- Return to the apex ($\sigma_1 = \sigma_2 = \sigma_3$)

In this paper, the detailed algorithmic procedures of returning to main plain 1, middle corner (only in UST model), and apex are derived as follows.

3.1. Return to the main plain 1

As shown in Figure 3, the constitutive relation can be written as follows:

$$\boldsymbol{\sigma} = \boldsymbol{\sigma}^{\text{trial}} - \Delta\lambda \boldsymbol{D}^{e}_{3\times 3} : \boldsymbol{N} \tag{3.1.1}$$

where $\boldsymbol{\sigma}^{\text{trial}}$ and $\boldsymbol{\sigma}$ are, respectively, the elastic trial principal stress vector and the updated principal stress vector; $\Delta\lambda$ is the plastic flow parameter; $\boldsymbol{D}^{e}_{3\times 3}$ is the reduced elastic isotropic constitutive matrix; and $\boldsymbol{N}$ is the reduced plastic flow vector normal to the main plane 1. The plastic flow vector $\boldsymbol{N}$ can be expressed as

$$\boldsymbol{N} = \begin{Bmatrix} 1 \\ -ab/(1+b) \\ -a/(1+b) \end{Bmatrix} \tag{3.1.2}$$

Substituting Equation (3.1.2) into Equation (3.1.1), the elasto-plastic stress–strain relationship can be rewritten as follows:

$$\sigma_1 = \sigma_1^{\text{trial}} - l\Delta\lambda \tag{3.1.3}$$

$$\sigma_2 = \sigma_2^{\text{trial}} - m\Delta\lambda \tag{3.1.4}$$

DOI: 10.1002/nme

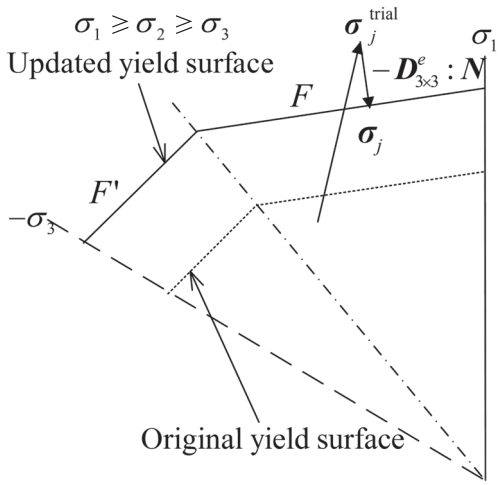

Figure 3. Return to main plane 1 in principal stress space.

$$\sigma_3 = \sigma_3^{\text{trial}} - n\Delta\lambda \tag{3.1.5}$$

where

$$l = (1-\alpha)K + \frac{2(2+\alpha)}{3}G$$
$$m = (1-\alpha)K + \frac{2(\alpha - 2\alpha b - b - 1)}{3(1+b)}G$$
$$n = (1-\alpha)K + \frac{2(\alpha b - 2\alpha - b - 1)}{3(1+b)}G$$

The updated stresses should lie on the yield surfaces. Substituting the constitutive function Equations (3.1.3)–(3.1.5) into Equation (3.1.1), one obtains with linear isotropic hardening

$$F : f^{\text{trial}} - \left(l - \frac{\alpha(bm+n)}{1+b} + H\right)\Delta\lambda = 0 \tag{3.1.6}$$

where $f^{\text{trial}} = \sigma_1^{\text{trial}} - \frac{\alpha}{1+b}(b\sigma_2^{\text{trial}} + \sigma_3^{\text{trial}}) - \sigma_t^0$, and H is the linear isotropic hardening modulus. From Equation (3.1.6), the plastic flow parameter can be derived as

$$\Delta\lambda = \frac{f^{\text{trial}}}{\left(l - \frac{\alpha(bm+n)}{1+b} + H\right)} \tag{3.1.7}$$

Substituting Equation (3.1.7) into Equations (3.1.3)–(3.1.5), respectively, the updated stresses can be easily obtained.

3.2. Return to the middle corner

As shown in Figure 4, the updated stresses lie on the middle corner Based on Koiter's theorem [7], the constitutive equation can be written as follows:

$$\boldsymbol{\sigma} = \boldsymbol{\sigma}^{\text{trial}} - \Delta\lambda^1 \boldsymbol{D}^e_{3\times3} : \boldsymbol{N} - \Delta\lambda^2 \boldsymbol{D}^e_{3\times3} : \boldsymbol{N}' \tag{3.2.1}$$

DOI: 10.1002/nme

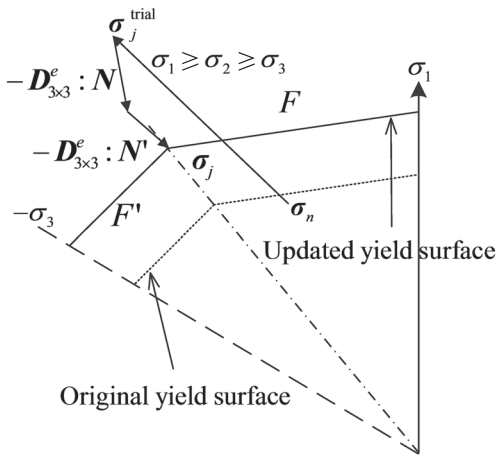

Figure 4. Return to the right corner in principal stress space.

where the plastic flow vectors $\boldsymbol{N}$ and $\boldsymbol{N}'$ are perpendicular to the main planes 1 and 2, respectively, and $\boldsymbol{N}'$ is given as

$$\boldsymbol{N}' = \begin{Bmatrix} 1/(1+b) \\ b/(1+b) \\ -a \end{Bmatrix} \tag{3.2.2}$$

Substituting Equations (3.1.2) and (3.2.2) into Equation (3.2.1), the constitutive equation at the middle corner can be represented as

$$\sigma_1 = \sigma_1^{\text{trial}} - l\Delta\lambda - l'\Delta\lambda' \tag{3.2.3}$$

$$\sigma_2 = \sigma_2^{\text{trial}} - m\Delta\lambda - m'\Delta\lambda' \tag{3.2.4}$$

$$\sigma_3 = \sigma_3^{\text{trial}} - n\Delta\lambda - n'\Delta\lambda' \tag{3.2.5}$$

where

$$l' = (1-\alpha)K + \frac{2(2+\alpha+\alpha b-b)}{3(1+b)}G$$

$$m' = (1-a)K + \frac{2(2b+\alpha+\alpha b-1)}{3(1+b)}G$$

$$n' = (1-\alpha)K - \frac{2(2\alpha+1)}{3}G$$

If the updated stresses lie on the middle corner, the consistency condition should be satisfied as follows:

$$F : f^{\text{trial}} - \left(l - \frac{\alpha(bm+n)}{1+b} + H\right)\Delta\lambda - (l' - \frac{\alpha(bm'+n')}{1+b} + H)\Delta\lambda' = 0 \tag{3.2.6}$$

$$F' : f'^{\text{trial}} - \left(\frac{l+bm}{1+b} - an + H\right)\Delta\lambda - \left(\frac{l'+bm'}{1+b} - an' + H\right)\Delta\lambda' = 0 \tag{3.2.7}$$

DOI: 10.1002/nme

where $f'^{\text{trial}} = \frac{1}{1+b}\left(\sigma_1^{\text{trial}} + b\sigma_2^{\text{trial}}\right) - a\sigma_3^{\text{trial}} - \sigma_t^0$. By solving the simultaneous Equations (3.2.6) and (3.2.7), the plastic flow parameters $\Delta\lambda$ and $\Delta\lambda'$ can be obtained as

$$\Delta\lambda = \frac{d' f^{\text{trial}} - d f'^{\text{trial}}}{c d' - c' d} \tag{3.2.8}$$

$$\Delta\lambda' = \frac{c f'^{\text{trial}} - c' f^{\text{trial}}}{c d' - c' d} \tag{3.2.9}$$

where

$$c = l - \frac{\alpha(bm+n)}{1+b} + H$$

$$d = l' - \frac{\alpha(bm'+n')}{1+b} + H$$

$$c' = \frac{l+bm}{1+b} - an + H$$

$$d' = \frac{l'+bm'}{1+b} - an' + H$$

Substituting Equations (3.2.8) and (3.2.9) into Equation (3.2.1), the explicit expression of updated stresses can be derived easily.

3.3. Return to the apex

The apex of UST model is the point along the hydrostatic axis ($\sigma_1 = \sigma_2 = \sigma_3$). Substituting $\sigma_1 = \sigma_2 = \sigma_3$ into Equation (2.1) or (2.2), the yield function at the apex can be rewritten as

$$(1-\alpha)\sigma_m = \sigma_t, \text{ when } \sigma_1 = \sigma_2 = \sigma_3 \tag{3.3.1}$$

where $\sigma_m = (\sigma_1 + \sigma_2 + \sigma_3)/3$. At the apex (Figure 5), the general constitutive equation for return mapping is given by Perić and Neto [16] as follows:

$$\sigma_m = \sigma_m^{\text{trial}} - K\Delta\varepsilon_{\text{V}}^p \tag{3.3.2}$$

where $\Delta\varepsilon_{\text{V}}^p$ is the volumetric plastic strain increment. For UST model, $\Delta\varepsilon_{\text{V}}^p$ is written as

$$\Delta\varepsilon_{\text{V}}^p = (1-a)\Delta\bar{\varepsilon}^p \tag{3.3.3}$$

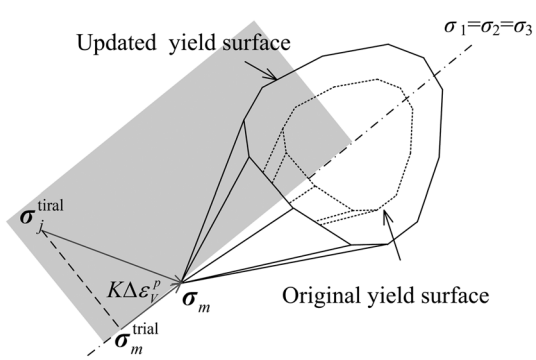

Figure 5. Return to the apex in principal stress space.

DOI: 10.1002/nme

where $\Delta\bar{\varepsilon}^p$ is the equivalent plastic strain increment. Substituting Equations (3.3.2) and (3.3.3) into Equation (3.3.1), one obtains

$$(1-\alpha)\sigma_m^{\text{trial}} - \sigma_t^0 - [K(1-a)^2 + H]\Delta\bar{\varepsilon}^p = 0 \tag{3.3.4}$$

Integrating Equations (3.3.2), (3.3.3), and (3.3.4), the explicit formulation of updated stresses is derived as follows:

$$\sigma_1 = \sigma_2 = \sigma_3 = \frac{H}{K(1-a)^2 + H}\sigma_m^{\text{trial}} + \frac{K(1-a)\sigma_t^0}{K(1-a)^2 + H} \tag{3.3.5}$$

The procedure of returning to main plain 2 is completely analogous to the procedure of returning to main plain 1, and the procedures of returning to the right and left corners are similar with Mohr–Coulomb's. They are, therefore, not necessary to be described again here.

4. CONSISTENT CONSTITUTIVE MATRIX FOR UNIFIED STRENGTH THEORY MODEL

It is known that the quadratic rate of convergence of Newton–Raphson iterations can be obtained by constructing the consistent constitutive matrix [18]. For a general return mapping algorithm based on principal stress space, the partial derivatives, $\partial\boldsymbol{\sigma}_j/\partial\boldsymbol{\varepsilon}_j^{e\,\text{trial}}$, of the principal stresses with respect to the principal elastic trial strains should be derived to assemble the consistent constitutive matrix.

In this paper, the consistent matrix for the main plane 1, middle corner, and apex of UST model is constructed in principal stress space.

4.1. Principal stress derivatives for the return mapping to main plane 1

For return mapping to main plane 1, differentiating Equation (3.1.1), it has

$$d\boldsymbol{\sigma} = d\boldsymbol{\sigma}^{\text{trial}} - d\Delta\lambda\boldsymbol{D}_{3\times3}^e : \boldsymbol{N} \tag{4.1.1}$$

where $d\boldsymbol{\sigma}^{\text{trial}} = \boldsymbol{D}_{3\times3}^e : d\boldsymbol{\varepsilon}^{\text{trial}}$. Similarly, by differentiating Equation (3.1.6), the linearized consistency condition is derived as follows:

$$df^{\text{trial}} - \left(l - \frac{\alpha(bm+n)}{1+b} + H\right)d\Delta\lambda = 0 \tag{4.1.2}$$

where $df^{\text{trial}} = d\sigma_1^{\text{trial}} - \frac{\alpha b}{1+b}d\sigma_2^{\text{trial}} - \frac{\alpha}{1+b}d\sigma_3^{\text{trial}}$. Combining Equations (4.1.1) and (4.1.2), the algorithmic tangent matrix for the return mapping to main plane 1 is obtained

$$\frac{\partial\boldsymbol{\sigma}_j}{\partial\boldsymbol{\varepsilon}_j^{\text{e trial}}} = \boldsymbol{D}_{3\times3}^e - \frac{\left(\boldsymbol{D}_{3\times3}^e : \boldsymbol{N}\right)\otimes\left(\boldsymbol{N}\boldsymbol{D}_{3\times3}^e\right)}{l - \frac{\alpha(bm+n)}{1+b} + H} \tag{4.1.3}$$

4.2. Principal stress derivatives for the return mapping to the middle corner

For return mapping to the middle corner, the incremental constitutive equation is derived from Equation (3.2.1) as follows:

$$d\boldsymbol{\sigma} = d\boldsymbol{\sigma}^{\text{trial}} - d\Delta\lambda\boldsymbol{D}_{3\times3}^e : \boldsymbol{N} - d\Delta\lambda'\boldsymbol{D}_{3\times3}^e : \boldsymbol{N}' \tag{4.2.1}$$

Differentiating Equations (3.2.8) and (3.2.9), one obtains

$$d\Delta\lambda = \left[\frac{d'\left(\boldsymbol{N} : \boldsymbol{D}_{3\times3}^e\right) - d\left(\boldsymbol{N}' : \boldsymbol{D}_{3\times3}^e\right)}{cd' - c'd}\right] : d\boldsymbol{\varepsilon}^{\text{trial}} \tag{4.2.2}$$

DOI: 10.1002/nme

$$d\Delta\lambda' = \left[\frac{c\left(\boldsymbol{N}' : \boldsymbol{D}^e_{3\times3}\right) - c'\left(\boldsymbol{N} : \boldsymbol{D}^e_{3\times3}\right)}{cd' - c'd}\right] : d\boldsymbol{\varepsilon}^{\text{trial}} \tag{4.2.3}$$

Substituting Equations (4.2.2) and (4.2.3) into Equation (4.2.1), the algorithmic tangent matrix for the return mapping to middle corner is derived as follows:

$$\begin{aligned}\frac{\partial\boldsymbol{\sigma}_j}{\partial}\boldsymbol{\varepsilon}_j^{\text{e trial}} = \boldsymbol{D}^e_{3\times3} - \left(\boldsymbol{D}^e_{3\times3} : \boldsymbol{N}\right) \otimes \left[\frac{d'\left(\boldsymbol{N} : \boldsymbol{D}^e_{3\times3}\right) - d\left(\boldsymbol{N}' : \boldsymbol{D}^e_{3\times3}\right)}{cd' - c'd}\right.\\ \left. - \left(\boldsymbol{D}^e_{3\times3} : \boldsymbol{N}'\right) \otimes \left[\frac{c\left(\boldsymbol{N}' : \boldsymbol{D}^e_{3\times3}\right) - c'\left(\boldsymbol{N} : \boldsymbol{D}^e_{3\times3}\right)}{cd' - c'd}\right]\right.\end{aligned} \tag{4.2.4}$$

4.3. Principal stress derivatives for the apex return

For return mapping to the apex, by differentiating Equation (3.3.5), one has

$$\frac{\partial\sigma_j}{\partial\varepsilon_j^{\text{e trial}}} = \frac{KH}{K(1-a)^2 + H} \tag{4.3.1}$$

for $i, j = 1, 2, 3$.

The derivation procedure of the matrix for main plane 2 is similar to the procedure for main plane 1, and the procedures for the right and left corners are analogous to the procedure for the middle corner. So, they are not described here again.

5. FLOWCHART OF THE INTEGRATION ALGORITHM FOR UNIFIED STRENGTH THEORY MODEL

With the possible return procedures at hand, it is necessary to determine which return mapping to apply in the actual numerical implementation of the model. The general method for choosing the proper return schemes is proposed by Perić and Neto [17]. In the present work, a similar method is established for UST model. Therefore, the details need not be given here, and the flowchart of the integration algorithm for UST model is only illustrated in Figure 6.

6. NUMERICAL EXAMPLES

6.1. Numerical testing of return mapping algorithm for unified strength theory model

In this section, the iso-error maps [19] are utilized to assess the accuracy of the proposed return mapping algorithm for UST model. In order to test the accuracy of the algorithm for all the surfaces, corners, and apexes of UST model, five starting points lying on the deviatoric plane for iso-error map are taken into account, which are illustrated in Figure 7.

The starting points A and B lie on the main planes 1 and 2, respectively. The starting points C, D, and E lie on the right, left, and middle corners, respectively. The elastic trial stress increment is expressed as follows:

$$\Delta\boldsymbol{\sigma}^{\text{trial}} = \Delta\sigma_N\boldsymbol{N} + \Delta\sigma_T\boldsymbol{T} \tag{6.1.1}$$

where $\boldsymbol{N}$ and $\boldsymbol{T}$ are the unit vectors, and $\Delta\sigma_N$ and $\Delta\sigma_T$ are the scalar factors. As shown in Figure 7, the unit vectors $\boldsymbol{T}$ are tangent to UST yield surfaces as well as normal to isocline for all five points. The vector $\boldsymbol{N}$ at the starting point A or B is normal to the main plane 1 or 2, respectively. And at the starting point C or D, vector $\boldsymbol{N}$ is chosen as the mean normal vector between the corresponding

DOI: 10.1002/nme

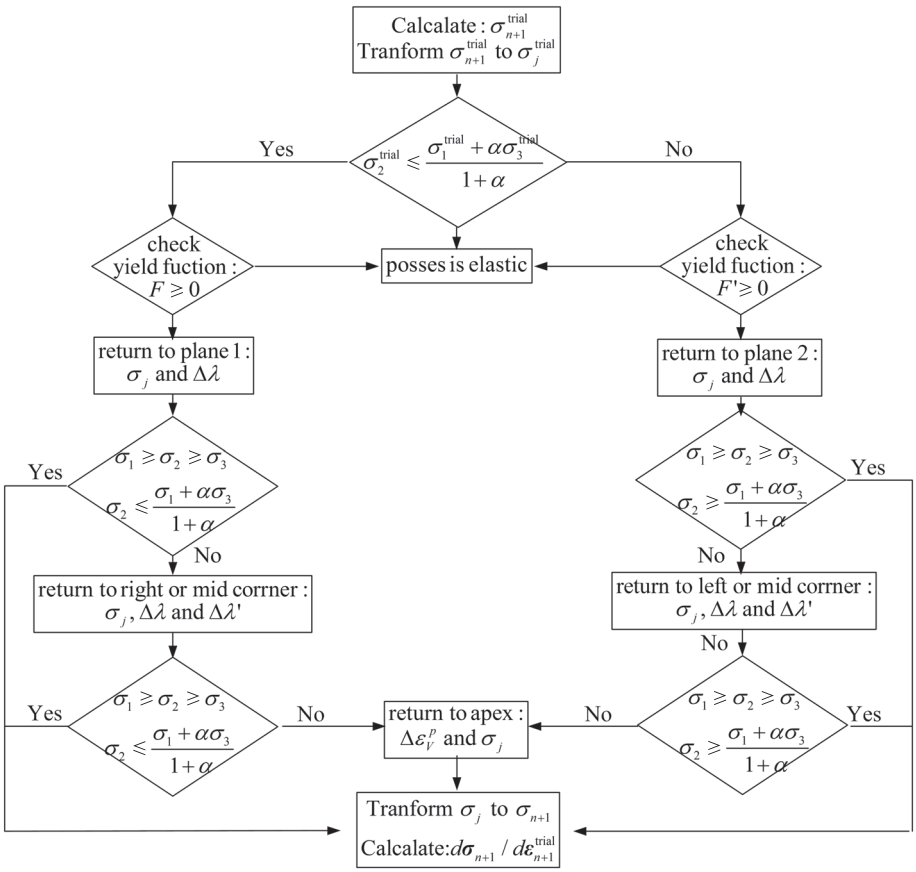

Figure 6. Flowchart of the integration algorithm for UST model.

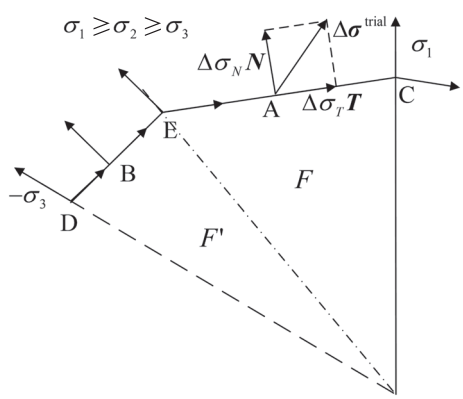

Figure 7. Iso-error maps for UST model and the increment directions.

adjacent planes. For the starting point E, the vector $\boldsymbol{N}$ is perpendicular to plain 2. The integration error can be defined as

$$error = \frac{\sqrt{(\boldsymbol{\sigma}^{\text{exact}} - \boldsymbol{\sigma}^{\text{num}}) : (\boldsymbol{\sigma}^{\text{exact}} - \boldsymbol{\sigma}^{\text{num}})}}{\sqrt{\boldsymbol{\sigma}^{\text{exact}} : \boldsymbol{\sigma}^{\text{exact}}}} \tag{6.1.2}$$

where the approximated stress $\boldsymbol{\sigma}^{\text{num}}$ is computed for each increment, and $\boldsymbol{\sigma}^{\text{exact}}$ is the exact stress obtained by 1000 sub-increments here. By varying values of $\Delta\sigma_N$ and $\Delta\sigma_T$, the iso-error maps

DOI: 10.1002/nme

for the five points are depicted, respectively, as shown in Figures 8–11. It is found that the integration error is little high only in some local narrow zones, and the integration error vanishes in the large area.

6.2. *Numerical simulation of three-point bending of rectangle beam*

Based on the user material subroutine (UMAT) interface requirement [20], the proposed return mapping algorithm for UST model with $b = 0/0.5/1$ is implemented in the ABAQUS 6.10 software (produced by Dassault Systèmes Simulia Corporation). Comparison of the results is carried out using the finite element (FE) simulation data of Mohr–Coulomb model built-in ABAQUS for the three-point bending test of square cross-section beam. The geometry of the beam is illustrated in Figure 12(a). Mohr–Coulomb strength theory can be written as

$$\frac{1}{2}(\sigma_1 - \sigma_3) + \frac{1}{2}(\sigma_1 + \sigma_3)\sin\varphi = c\cos\varphi \tag{6.2.1}$$

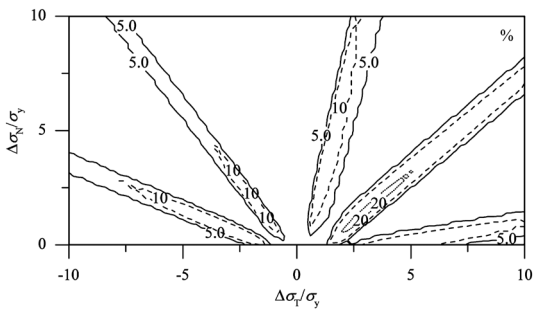

Figure 8. Iso-error map of starting point A.

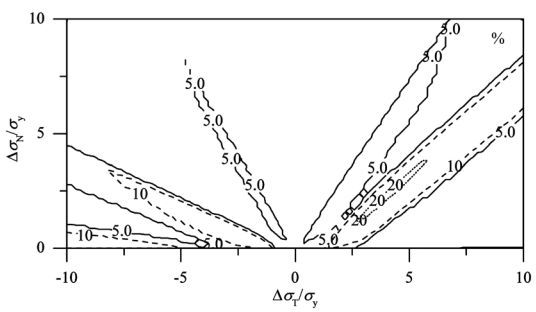

Figure 9. Iso-error map of starting point B.

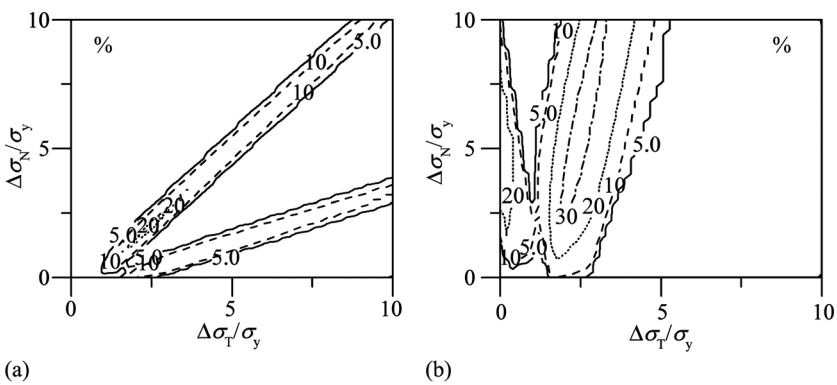

Figure 10. Iso-error map of starting points (a) C and (b) D.

DOI: 10.1002/nme

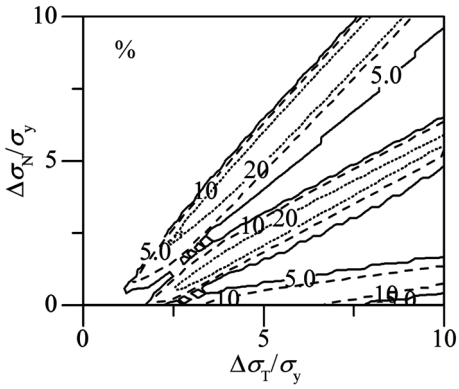

Figure 11. Iso-error map of starting point E.

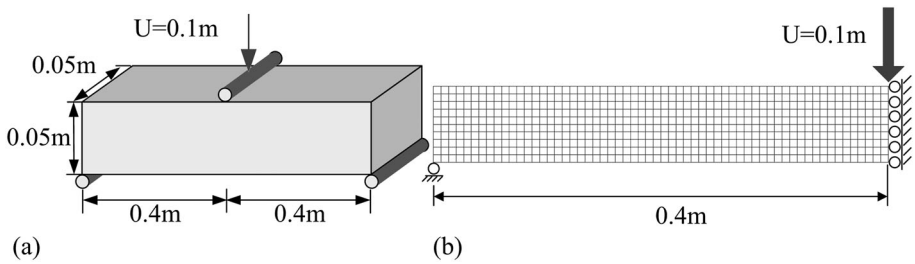

Figure 12. Three-point bending test: (a) geometry and (b) FE mesh.

where c is the cohesion force and φ is the internal friction angle. Alternatively, Equation (6.2.1) can be rewritten as

$$\sigma_1 - a\sigma_3 = \sigma_t \tag{6.2.2}$$

$$a = \frac{1 - \sin\varphi}{1 + \sin\varphi} \tag{6.2.3}$$

$$\sigma_t = \frac{2c\cos\varphi}{1 + \sin\varphi} \tag{6.2.4}$$

The elastic parameters used in this problem are Young's modulus $E = 10$ GPa and Poisson ratio $v = 0.2$. UST material constants are given as follows: the tensile and compressive strength ratio $\alpha = 0.25$, the influence coefficient of the intermediate principal stress $b = 0/0.5/1$, and the tensile strength $\sigma_t = 30$ MPa. The corresponding internal friction angle is $\varphi = 37°$, and the cohesion force is $c = 30$ MPa, respectively.

Only half of the beam is modeled in the FE simulation due to the symmetry, and the displacement control is adopted to apply the loading in five increments with equal size. Under the assumption of ideal elastic–plastic material ($H = 0$), and linear hardening material ($H = 100$ MPa), two analyses are carried out using eight-node linear-brick full integration element. The FE mesh consists of 3200 elements with 76,800 degrees of freedom. The FE mesh model and boundary conditions are shown in Figure 12(b).

In Figure 13(a) and 13(b), the displacement versus load curves from the present model are compared with the simulation results of the ABAQUS for ideal elastic–plastic material and linear hardening material, respectively. Complete agreement between the result of the present model with $b = 0$ and the result of the ABAQUS is observed, which demonstrates the accuracy of the proposed

DOI: 10.1002/nme

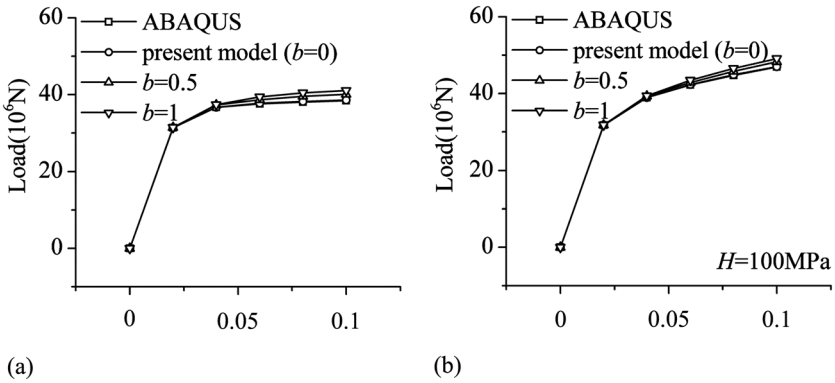

Figure 13. Load-displacement relation for (a) ideal elastic–plastic and (b) linear hardening.

Table I. The evolution of the largest residual force factor for the simulation of the three-point bending test.

Number of iterations	Largest residual force factor							
	$H = 0$				$H = 100$ MPa			
	ABAQUS	$b = 0$	$b = 0.5$	$b = 1$	ABAQUS	$b = 0$	$b = 0.5$	$b = 1$
1	0.54489	2.9832	0.8956	1.7183	0.98336	0.9015	0.9387	0.5313
2	0.09914	0.5819	0.2189	0.2738	0.425139	0.2900	0.04903	0.1200
3	0.02209	0.1602	0.1390	0.00066	0.13486	0.01101	0.00977	0.0099
4	0.03142	0.01725	0.01002	—	0.02155	0.00207	3.1E-05	9.2E-07
5	0.00793	0.00161	1.04E-05	—	0.00753	—	—	—
6	0.01426	—	—	—	0.00256	—	—	—
7	0.0032	—	—	—	—	—	—	—

return mapping algorithm for UST model. In addition, the load increases with the value of b for constant displacement.

According to the convergence criterion for the solution of nonlinear problems defined in the ABAQUS/Standard, if the ratio of the largest residual force to the time-averaged force (we call it largest residual force factor in this paper) is less than the convergence tolerance 0.5% during Newton–Raphson iterations, the convergence check is satisfied [21]. The evolution of the largest residual force factor with Newton–Raphson iterations using the Mohr–Coulomb model the built-in ABAQUS and the present UST model with $b = 0/0.5/1$ for the fifth increment step are listed in Table I.

It can be observed that the convergence rate of the return mapping algorithm for UST model is quadratic. Furthermore, it is seen that the convergence speed of the present model with $b = 0$, 0.5, 1 appears to be higher than that of the built-in Mohr–Coulomb model of the ABAQUS.

6.3. Numerical simulation for the behavior of internally pressured cylinder

To take $b \neq 0$ into account, the simulation of the perfect elasto-plastic deformation of a long thick-walled cylinder under internal pressure is carried out. The problem's geometry and the corresponding FE mesh model are illustrated in Figure 14, and the material parameters are listed in Table II.

Under the assumption of plane strain condition, the four-node bilinear plane strain full integration element is used in the FE analysis. Because of symmetry, only a quarter of cylinder cross section is applied to FE simulation with the appropriate displacement constraint as shown in Figure 14(b). The FE mesh consists of 897 elements with 7176 degrees of freedom. The pressure $P = 1.1645$ KPa, prescribed on the inner surface, is applied to loading in one single step. The contour plots of the hoop stress with the present model are illustrated in Figure 15.

DOI: 10.1002/nme

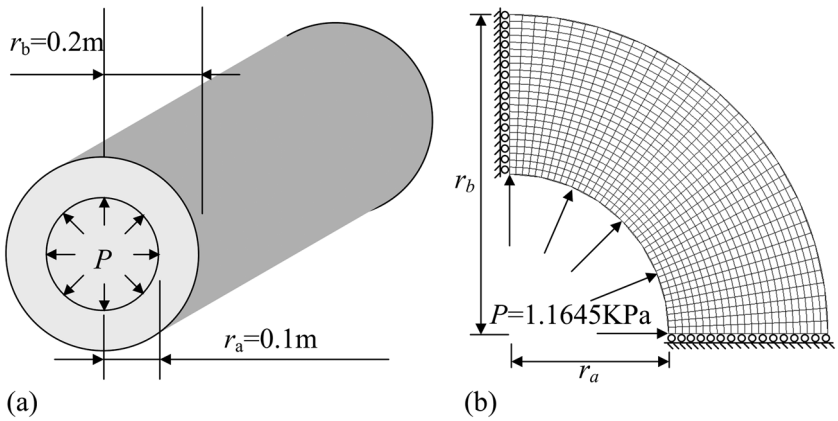

Figure 14. Internal pressured cylinder: (a) geometry and (b) FE mesh.

Table II. Material parameters.

E (MPa)	v	α	b	σ_t
240	0.2	0.49	0/0.5/1	1.4 KPa

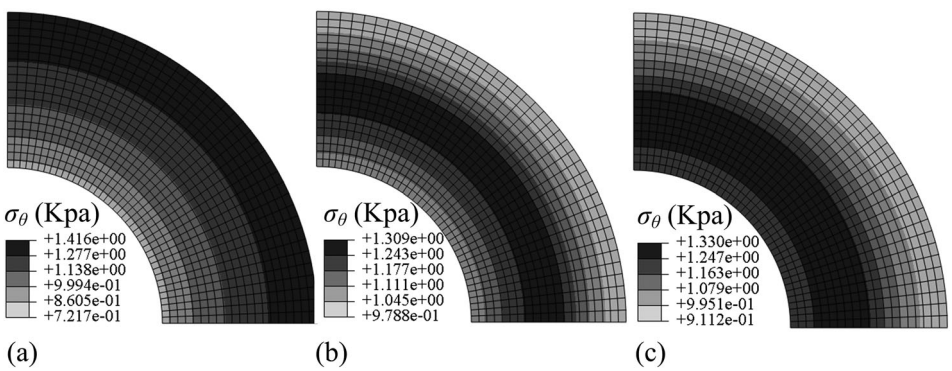

Figure 15. Contour plots of hoop stress with (a) $b = 0$, (b) $b = 0.5$, and (c) $b = 1$.

A closed-form solution to this problem with UST has been derived by Yu [9]. The hoop stress computed by the present method is plotted in the radial direction as illustrated in Figure 16, and it is in complete agreement with the closed-form solution.

The corresponding evolution of the largest force factor with Newton–Raphson iterations using the present model with $b = 0/0.5/1$ is listed in Table III.

By simulating the behavior of the long thick-walled cylinder subjected to internal pressure, we can find that the FE result is in very good agreement with the theoretical solution. It indicates the correctness of the present numerical model.

6.4. Numerical simulation for slope stability

In this section, a slope stability analysis under gravity is considered as a more general example. The perfect plasticity with no-hardening is assumed here. The problem's geometry and boundary conditions are illustrated in Figure 17, and the corresponding material parameters are listed in Table IV.

Taking into account Equations (6.2.3) and (6.2.4), corresponding Mohr–Coulomb model parameter can be calculated, i.e., the internal friction angle $\varphi = 20°$ and the cohesion $c = 12.38$ KPa,

DOI: 10.1002/nme

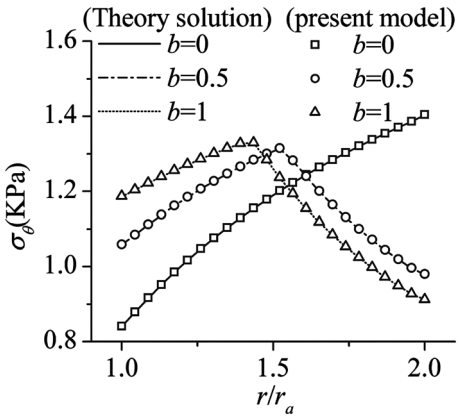

Figure 16. Hoop stress distribution when $b = 0$, 0.5, and 1.0.

Table III. The evolution of the largest residual force factor for the simulation of thick-walled cylinder under internal pressure.

Number of iterations	Largest residual force factor		
	$b = 0$	$b = 0.5$	$b = 1$
1	0.66541	0.29415	0.14238
2	0.32493	0.05661	0.03585
3	0.16806	0.00381	0.00243
4	0.08318	—	—
5	0.03008	—	—
6	0.00719	—	—
7	0.0063	—	—
8	1.47704E-6	—	—

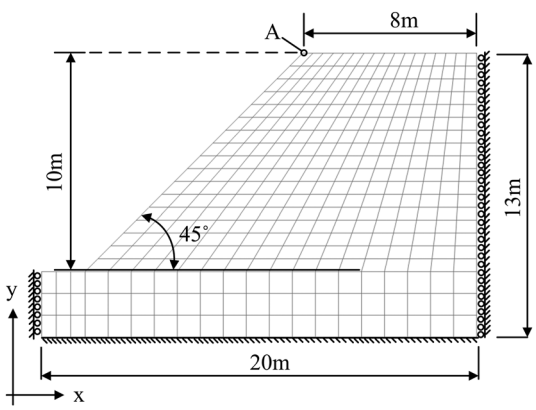

Figure 17. Slope stability analysis under gravity: geometry and boundary conditions.

respectively, while $b = 0$. According to the limit analysis of slope under gravity given by Chen [22], if the ratio

$$N = h\frac{\gamma}{c} \tag{6.4.1}$$

reaches the critical value N_s, which is called the stability factor, the slope will collapse. The $h = 10$ m and $\gamma = 20$ KN/m^3, in Equation (6.4.1), are the height and the unit weight of the slope, respectively. With the geometry properties as shown in Figure 17 and material parameters of slope

DOI: 10.1002/nme

Table IV. Material parameters.

E (MPa)	v	α	b	σ_t
100	0.35	0.4903	0/0.25/0.5/0.75/1	17.34 KPa

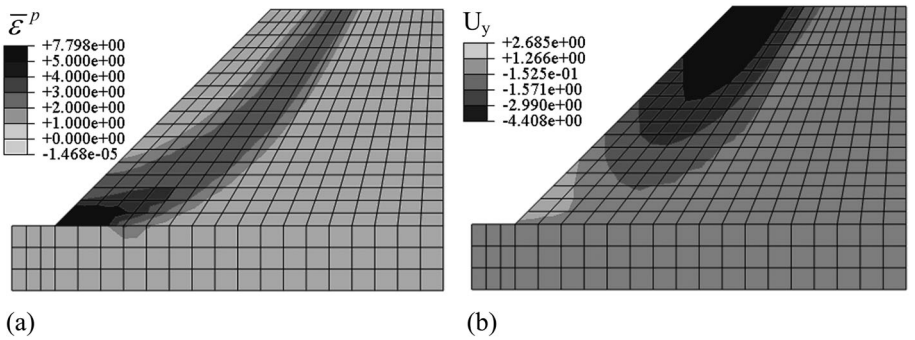

Figure 18. Contour plot of (a) equivalent plastic strain and (b) displacement in y-direction at collapse with $b = 0$.

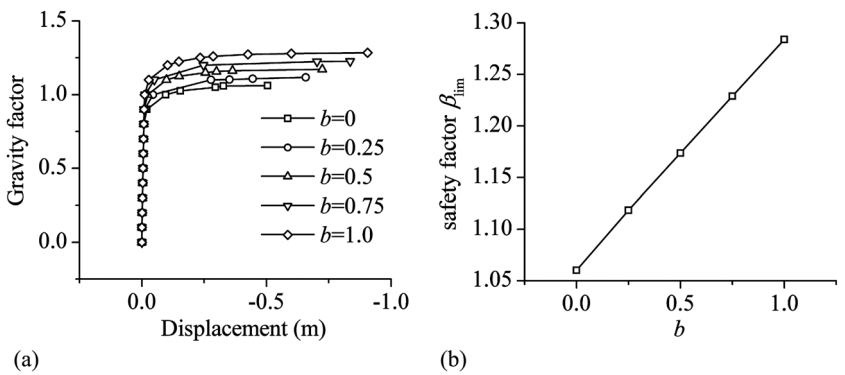

Figure 19. (a) Evolution of displacement in y-direction for point A with gravity factor and (b) evolution of safety factor with parameter b.

in Table IV, the stability factor $N_s \approx 16.16$ according to the limit analysis solution by Chen, which is almost equal to the ratio $N \approx 16.155$, calculated from Equation (6.4.1). The corresponding safety factor β_{lim} according to slope stability analysis can be defined as $N_s/N \approx 1$.

In FE simulation for this problem, the unit weight γ is considered as the gravity loading, i.e., $\bar{\gamma} = \beta\gamma$. The gravity factor β is increased linearly until the slope instability occurs. The corresponding mesh model, as shown in Figure 17, consists of 349 four-node plane strain elements with 4188 degrees of freedom. In accordance with the built-in automatic step size adjustment of the ABAQUS, the pseudo-time period of the simulation is set to be 2, and the initial increment step size is equal to the maximum increment step size and set to be 0.1. In order to obtain the accurate value of safety factor, the minimum increment step size is set to be 1×10^{-5}. The contour plot of equal plastic strain and displacement in y-direction (as shown in Figure 17) at collapse with $b = 0$ is illustrated in Figure 18(a) and 18(b). The evolution of displacement in y-direction for point A (as shown in Figure 17) with the gravity factor β, using the present model with $b = 0/0.25/0.5/0.75/1$, is plotted in Figure 19. In addition, the evolution of the largest force factor with Newton–Raphson iterations using the present model with $b = 0/0.25/0.5/0.75/1$ for the 10th increment step is listed in Table V.

As shown in Figure 19(a), the displacement in y-direction at point A increases suddenly when the gravity factor reaches 1.06 with $b = 0$. It indicates that the slope instability occurs. Therefore, the

DOI: 10.1002/nme

Table V. The evolution of the largest residual force factor for the slope stability analysis.

Number of iterations	Largest residual force factor				
	$b = 0$	$b = 0.25$	$b = 0.5$	$b = 0.75$	$b = 1$
1	3.26205	2.75226	2.25575	1.25061	0.75949
2	2.55775	1.32367	0.79872	0.4084	0.12944
3	1.7415	1.07006	0.40208	0.18848	0.01757
4	1.00545	0.62799	0.30604	0.09709	0.00116
5	0.37982	0.36398	9.81E-02	0.00586	—
6	0.04887	0.10852	0.04604	2.51E-05	—
7	0.00487	0.01686	3.57E-04	—	—
8	—	7.91E-05	—	—	—

safety factor β_{lim} with $b = 0$ is equal to 1.06, which is 6% above the limit analysis solution. Also, more exhaustive results can be obtained with the variation of b, which is different from the limiting case using Mohr–Coulomb model, and the values of the safety factor β_{lim} increase with increasing of b as shown in Figure 19(b).

7. CONCLUSIONS

A return mapping algorithm in principal stress space for UST model is presented. In contrast to the Mohr–Coulomb and Tresca models, the UST model contains two planes and three corners in the sextant of principal stress space, and the apex is formed by the intersection of 12 corners rather than the six corners of Mohr–Coulomb in the whole principal stress space. The general return mapping algorithm in principal stress space is established for UST model, and the corresponding consistent constitutive matrices in principal stress space are constructed too.

With the iso-error maps, the present model is assessed to be accurate for dealing with the return mapping at all planes, corners, and apexes. And the correctness and flexibility of the present numerical model are also demonstrated by comparing some FE results with the result from the commercial software ABAQUS and the analytical result, respectively.

ACKNOWLEDGEMENTS

This work was supported by the National Basic Research Program of China (no. 2013CB035704) and the National Nature Science Foundation of China (no. 11472206).

REFERENCES

1. Colmenares LB, Zoback MD. A statistical evaluation of intact rock failure criteria constrained by polyaxial test data for five different rocks. *International Journal of Rock Mechanics and Mining Sciences* 2002; **39**(6):695–729.
2. Michelis P. Polyaxial yielding of granular rock. *Journal of Engineering Mechanics* 1985; **111**(8):1049–1066.
3. Willam KJ, Warnke EP. Constitutive model for the triaxial behavior of concrete. *Proceedings of IABSE Seminar on Concrete Structures Subjected to Triaxial Stress*, Vol. 19, Bergamo, Italy, 1975; 1–30.
4. Hoek E, Carranza-Torres C, Corkum B. Hoek-Brown failure criterion-2002 edition. *Proceedings of NARMS-TAC*, Vol. 1, Toronto, Canada, 2002; 267–273.
5. Lade PV, Duncan JM. Elastoplastic stress-strain theory for cohesionless soil. *Journal of the Geotechnical Engineering Division* 1975; **101**(10):1037–1053.
6. Yu MH. *Unified Strength Theory and its Applications*. Springer-Verlag: Berlin, Heidelberg, 2004. DOI: 10.1007/978-3-642-18943-2.
7. Koiter WT. Stress–strain relations, uniqueness and variational theorems for elastic–plastic materials with a singular yield surface. *Quarterly of Applied Mathematics* 1953; **11**(3):350–354.
8. Abbo AJ, Sloan SW. A smooth hyperbolic approximation to the Mohr–Coulomb yield criterion. *Computers & Structures* 1995; **54**(3):427–441.
9. Yu MH, Ma GW, Qiang HF, Zhang YQ. *Generalized Plasticity*. Springer-Verlag: Berlin, Heidelberg, 2006. DOI: 10.1007/3-540-30433-9.
10. Ma ZY, Liao HJ, Dang FN. Unified elastoplastic finite difference and its application. *Applied Mathematics and Mechanics* 2013; **34**(4):457–474.

11. Pankaj BN, Detection of multiple active yield conditions for Mohr–Coulomb elasto-plasticity. *Computers & Structures* 1997; **62**(1):51–61.
12. Larsson R, Runesson K. Implicit integration and consistent linearization for yield criteria of the Mohr–Coulomb type. *Mechanics of Cohesive-frictional Materials* 1996; **1**(4):367–383.
13. Perić D, Neto EA. A new computational model for Tresca plasticity at finite strains with an optimal parametrization in the principal space. *Computer Methods in Applied Mechanics and Engineering* 1999; **171**(3):463–489.
14. Borja RI, Sama KM, Sanz PF. On the numerical integration of three-invariant elastoplastic constitutive models. *Computer Methods in Applied Mechanics and Engineering* 2003; **192**(9):1227–1258.
15. Clausen J, Damkilde L, Andersen L. Efficient return algorithms for associated plasticity with multiple yield planes. *International Journal for Numerical Methods in Engineering* 2006; **66**(6):1036–1059.
16. Clausen J, Damkilde L. An exact implementation of the Hoek–Brown criterion for elasto-plastic finite element calculations. *International Journal of Rock Mechanics and Mining Sciences* 2008; **45**(6):831–847.
17. de Souza Neto EA, Peric D, Owen DRJ. *Computational Methods for Plasticity: Theory and Applications.* John Wiley & Sons: Chichester, United Kingdom, 2008. DOI: 10.1002/9780470694626.
18. Simo JC, Hughes TJR. *Computational Inelasticity*. Springer-Verlag: Berlin, Heidelberg, 1998.
19. Ortiz M, Popov EP. Accuracy and stability of integration algorithms for elastoplastic constitutive relations. *International Journal for Numerical Methods in Engineering* 1985; **21**(9):1561–1576.
20. Hibbitt H, Karlsson B, Sorensen P. *Abaqus User Subroutines Reference Manual Version 6.10*. Dassault Systèmes Simulia Corp.: USA, 2011.
21. Hibbitt H, Karlsson B, Sorensen P. *Abaqus Analysis User's Manual Version 6.10*. Dassault Systèmes Simulia Corp.: USA, 2011.
22. Chen WF. *Limit Analysis and Soil Plasticity*. Elsevier: Amsterdam, 1975.